20th AIAA Computational Fluid Dynamics Conference
27 - 30 June 2011, Honolulu, Hawaii

AIAA 2011-3204

Fully-resolved LES of weakly separated flows

Peter A. Chang, III,*
Abel Vargas,†Minyee Jiang,‡Dory Lummer,§
and
Krishnan Mahesh,¶

Abstract

A high-accuracy large eddy simulation (LES) is applied to flows over a sphere and an underwater vehicle. Both objects have relatively weak separated stern flows that may depend upon the accurate resolution of turbulence structures in the attached flow regions upstream of the separation point. For the sphere we compute flows over a range of Reynolds numbers from sub- to super-critical ($Re = 1\times10^4$ to $Re = 1.14\times10^6$, respectively) for which we obtain decent agreement for the separation location, pressure distributions and integrated forces. Long time series data shows evidence of low-frequency shedding phenomena. We perform LES on the Advanced SEAL Delivery System (ASDS), an underwater vehicle with a rounded-rectangular cross section and stern slope that promotes weak flow separations. We compute the fully resolved flow over the ASDS for length-based Reynolds numbers 128×10^3, 256×10^3 and 512×10^3. We show that the mean flow fields over the attached flow region are reasonable in that the boundary layer profiles, shape factors and skin friction agree with other examples of developing turbulent boundary layer flows. The instantaneous flow fields exhibit near-wall turbulence structures with the correct length scales and dynamics as compared with the wall-bounded turbulent flow literature. The separation point moves aft and the extent of the separation region decreases markedly as the Reynolds number increases.

Nomenclature

A_s	Surface area of sphere, m^2
C_D	Integrated drag coefficient, $F_x/(0.5\rho U_o^2 A_s)$
C_f	Local drag coefficient, $\tau_w/(0.5\rho U_o^2)$
C_p	Pressure coefficient, $p/(0.5\rho U_o^2)$
D	Sphere diameter, m
$F_{x,y,z}$	Force in streamwise, spanwise and vertical directions, N
h	Height of ASDS parallel middle body normalized by ℓ_{gu}
H	Boundary layer shape factor
ℓ_{gu}	Length of grid unit for ASDS, 5.08 cm
p	Pressure, N/m^2
r, R	Radii of ring-torus topology as described in the sphere results section.
Re_L	Reynolds number for ASDS based on total length and free stream velocity.
Re_x	Reynolds number for ASDS based on distance from bow and free stream velocity.
Re_{δ^*}	Reynolds number for ASDS based on displacement thickness and free stream velocity.

*Corresponding author. Email: peter.chang@navy.mil, Computational Hydromechanics Division, Naval Surface Warfare Center — Carderock Division (NSWCCD), West Bethesda, MD 20817. Senior Member.
†Computational Hydromechanics Division, NSWCCD, West Bethesda, MD 20817, non-member.
‡Computational Hydromechanics Division, NSWCCD, West Bethesda, MD 20817, non-member.
§Computational Hydromechanics Division, NSWCCD, Member.
¶Professor, Dept. of Aerospace and Mechanical Engineering, University of Minnesota, Minneapolis, MN, 55455, Associate Fellow

Re_θ Reynolds number for ASDS based on momentum thickness and free stream velocity.
St Strouhal number
U_o Freestream velocity, m/s
w Width of ASDS parallel middle body, m
β Side force angle, ^{o}
δ Boundary layer thickness, cm
Δ^+ Viscous unit, ν/u_τ, cm
λ_2 2nd invariant of the strain rate tensor
ϕ Polar angle on sphere with respect to incoming flow, ^{o}
θ Azimuthal angle for sphere, ^{o}
θ Angle of ASDS afterbody, ^{o}
x Computational axial coordinates in grid units, positive in flow direction
ξ Axial coordinates with respect to bow in grid units, positive in flow direction
L_a Length of ASDS in grid units
ζ Spanwise coordinate with respect to ASDS z-centerplane in grid units
η Vertical coordinate with respect to ASDS y-centerplane in grid units
τ_w Shear stress at the wall, N/m^2
u_τ Shear velocity, m/s

I. Introduction

MANY high Reynolds number flows of practical interest such as those about submarines and submersibles, feature an upstream section of attached flow leading to a stern region where the flow weakly separates. These types of flows are much different than what can be termed as strongly separated flows such as backward facing steps, airfoils at large angles of attack, square cylinders and circular cylinders. In strongly separated flows geometric discontinuities set up strong shear flows that generate Kelvin-Helmholtz vortices and periodic shedding. Since the turbulence generation mechanisms are due to strong shear layer interactions, it is debatable whether the separation dynamics depend to any great extent on the upstream wall-bounded turbulence. On the other hand, weakly separated flows, at least for the purposes of this paper, have very weak shear layer turbulence generation and therefore, the turbulence in the upstream attached flow regions may play an important role in determining when separation will occur and once separated, the dynamics of the separated flow region. As we will show in this paper these weakly separated flows typically do not have a preferred shedding frequency e.g., as a circular cylinder would, because the separations are highly three-dimensional and spanwise shed vortices are not well developed. In this paper we document the application of a high-accuracy LES methodology for the flow over a sphere and a small submersible, both of which have weakly separated flows.

A. Sphere

The flow over a sphere is reasonable weakly separated flow test case because of its geometric simplicity and the fact that it has a three-dimensional wake, much like the ASDS. For smooth spheres in the range $2 \times 10^3 < Re < 3.7 \times 10^5$ the flow is "sub-critical", where the flow on the sphere is laminar with the flow transitioning to turbulence in the wake. The flow separates early due to the laminar velocity profile's susceptibility to separation. Above about 3.7×10^5 the flow on the sphere becomes "super-critical" where the flow transitions to turbulence on the sphere surface, and therefore, the flow separates further around the sphere. Schlichting[1] shows that for $2 \times 10^3 < Re < 3.7 \times 10^5$ the drag coefficient is a constant at about $C_D \approx 0.4$. For $Re > 3.7 \times 10^5$ the drag drops precipitously to about $C_D = 0.09$ before increasing slowly with Reynolds number. Achenbach[2] show that in the sub-critical range the flow has a narrow-band peak for which the Strouhal number increases from 0.125 to 0.18 over the range $6 \times 10^3 < Re < 3 \times 10^4$. For $Re > 3 \times 10^4$, $St \approx 0.18$. For $Re > 3.7 \times 10^5$, no shedding peak is detected.

Constantinescu and Squires,[3] referred to as "CS" for the remainder of the paper, performed a detached eddy simulation (DES) on a sphere with structured grids over a range of sub- and super-critical Reynolds numbers ($Re = 1 \times 10^4$ and $Re = 1.14 \times 10^6$, respectively) investigating the physics of the wake. CS used a number of numerical treatments: on the sphere the turbulence was modeled using the Spalart-Allmaras

turbulence model and the advective terms in the momentum equations were 5th order upwind. Upwinding is also used in the "small upstream part of the detached shear layers," ostensibly where, for the sub-critical case, the flow is transitioning to turbulence. In the wake second order central differencing was used and the turbulence model reverts to a Smagorinsky sub-grid scale model.

Kim[4] performed LES on a sphere with unstructured grids using a "bounded" second order central difference scheme on the advective terms in the momentum equation. In this method oscillations that are smaller than the twice the grid size are truncated resulting in a much more stable calculation. A localized dynamic k_{sgs}-equation model is used for the SGS stresses. Kim performs a fully-resolved LES for $Re = 10^4$ and using the same unstructured grid performs a simulation at $Re = 1.14 \times 10^6$ using a "blended" law of the wall.

B. ASDS

The ASDS is a convenient hull shape to develop LES methodology for separated flows because it features a prismatic upstream hull where the attached flow should undergo boundary layer development, a knuckle where the flow will accelerate and then a sloping stern where an adverse pressure gradient and weak flow separation will develop. In this investigation we fully-resolve the flows in the upstream attached region. That we need to resolve the near-wall turbulence is based on earlier work by Chang et al.[5] who compared vortex shedding from a weakly shedding NACA 0016 hydrofoil comparing fully-resolved LES and LES with wall models. They found that the vortex shedding peak was not resolved with the wall model concluding that the resolved wall-bounded turbulence makes up a significant portion of the energy in the separated flow region. They showed that the quasi-streamwise vortices that inhabit the near-wall layers in the attached flow region are engulfed by the Kelvin-Helmholtz vortices greatly augmenting their strength.

To our (limited) knowledge there is no turbulence simulation work being done on weakly shedding flows like ASDS. The Ahmed body[6] is a hatchback automobile geometry that shares some similarities to ASDS in that it has a region of attached flow and a downstream flow region where the flow is weakly separated. The major difference however, is that the parallel middle body and the stern hatchback section are separated by an abrupt slope discontinuity. The roof and sides also have slope discontinuities and furthermore, the back of the vehicle is abruptly terminated. These features tend to promote strong shear layers which may allow for the development of massive separations and turbulent wake flows without the resolution of wall-bounded turbulence upstream. Many LES studies have been performed on the Ahmed body, for example by Minguez et al,[7] Hinterberger,[8] and Howard and Pourquie.[9] These LES investigations have not resolved the near-wall turbulence, using wall models to model the boundary layer in the attached flow regions. The grid sizes have been relatively small (around 20×10^6 cells).[7,8] The fact that the LES studies mentioned above employed wall modeling techniques may have contributed to the under- (Howard and Pourquie[9]) and over- (Minguez et al.[7]) prediction of drag. Krajnovic and Davidson[10] mentions that 600 million cells would be required in the near wall region to fully resolve all scales in the Ahmed body at $Re = 5 \times 10^6$.

Other LES work on simplified ground vehicles with a squared back end has focused on the introduction of drag-reduction devices attached to the back end of the model,[11] and capturing flow structures that develop on the blunt front end and as the flow detaches from the body.[12] Again these studies are not directly applicable to ASDS as they have a much blunter nose which generates strong leading edge separation.

LES of streamlined bodies with completely attached flow is the another avenue that has been investigated. Since these flows are attached they are more amenable to use of wall layer models. Well-resolved LES is only necessary in the stern where e.g., turbulence fluctuations are necessary for hydro-acoustics. Alin et al[13] investigated the flow over barehull and fully-appended SUBOFF model at $Re = 12 \times 10^6$ (based on length) using the OpenFOAM LES solver. In this case they used up to 56×10^6 cells obtaining reasonable results for the mean flows.

In this paper we first describe the computational method; we then describe the sphere and ASDS geometry and computational grids; we then show results for the sphere and ASDS and compare to available experimental data and previous computations. For the sphere calculations we perform simulations over a range of sub- and super-critical Reynolds numbers on a single mesh that is wall-resolved for the sub-critical cases. Therefore, the super-critical cases are under-resolved. Nonetheless, the results, as compared to available experimental and computational data, are quite satisfactory. Since we are able to run for longer time periods than seen in the literature we shed some light on low-frequency phenomena such as wake rotation. It is acknowledged that wall-resolved super-critical simulations need to be performed to fully confirm our findings. For ASDS we perform simulations on three grids in which the Reynolds number is increased by a factor of two for each and the grids for each are refined such that the wall-bounded flows remain fully-resolved

(by LES standards, anyway). The ASDS simulations are meant to be exploratory in nature investigating the practicality of the running problems with over 100×10^6 cells. Also, there is very little experimental data for ASDS at our Reynolds numbers so we show results that demonstrate that the solutions are reasonable.

II. Mathematical Formulation

We are using the LES code MPCUGLES (Massively Parallel Computations on Unstructured Grids LES). The incompressible LES equations are obtained by spatially filtering the Navier-Stokes equations assuming that the filtering operation commutes with the spatial and temporal derivatives. The dynamic sub-grid scale (SGS) model of Germano et al.,[14] modified by Lilly,[15] is used to model the SGS stresses. The filtered momentum equations are solved using a numerical method developed by Mahesh et al.[16] for incompressible flows on unstructured grids. The finite volume algorithm, derived to be robust with minimal numerical dissipation, stores the Cartesian velocities and pressures at the control volume (CV) centroids with the face-normal velocities stored independently at the centroids of the faces. A predictor-corrector approach is used where the predicted velocities at the CV centroids are first obtained, then interpolated to obtain the face-normal velocities. The predicted face-normal velocity is projected such that continuity is discretely satisfied. This yields a Poisson equation for pressure, which is solved by algebraic multi-grid (AMG)[17] or conjugate gradient (CG) approaches. The pressure field is used to update the Cartesian CV velocities using a least-squares formulation that is essential for obtaining solutions on highly skewed grids. Time advancement is performed using an implicit Crank-Nicholson scheme. Chang et al.[18] compare the speedups for solving large problems on massively parallel compute clusters using CG and AMG methods showing that for a 13 million CV propeller crashback problem, using the CG Poisson solver, the code has near linear speed up for up to 400 processors.

III. Geometry and Grids

A. Sphere

For the sphere we utilized a hybrid mesh topology consisting of prisms, tetrahedra, pyramids and hexahedra as shown in Figure 1. This topology was used because the region of tets would allow for the potential development of grids around complex structures such as ASDS with support pylons and for multiple interacting bodies. Several meshes were generated to compare the effects of surface mesh size, wall-normal spacing and grid density in the wake region. Figure 2(a) shows that the surface of the sphere is covered with triangles (120 triangles around the sphere circumference) with 36 prism layers extending $0.284D$ off the wall. The wall normal distance to the first cell boundary is $1.1 \times 10^{-3}D$. Based on the estimate that $u_\tau = 0.04U_o$, the grid wall-normal spacing at the wall is $0.44\Delta^+$ for $Re = 1 \times 10^4$, $1.8\Delta^+$ for $Re = 4.8 \times 10^4$ and $48\Delta^+$ for $Re = 1.12 \times 10^6$. Thus, it is known a priori that the boundary layer flows for the super-critical cases are under resolved. As will be shown in the results section the physics of the super-critical cases appear to be correct despite this under resolution. The reason may be that the wake dynamics drive many of the important physical processes for this problem.

Prism layers are grown off the sphere until a unit cell aspect ratio is achieved. Outside of the prism layers the tets have approximately the same length scales giving a very small cell growth rate. The tet region is a cylinder that that was sized such that it would contain the velocity fluctuations in a relatively constant cell-size region as shown in Figure 1(a). At the outer boundary of the tet cylinder a layer of pyramids provides a transition to the outer hex region. The hex region outside allows for efficient cell size growth to the outer boundaries. A constant-x cut for Sphere-2, downstream of the sphere body shows the transition from the inner tet region to the outer hex region. The inflow plane is located at $x = -14.5D$ and the outflow boundary at $20.5D$. The cylindrical outer boundary is located at $14.5D$ from the sphere centerline. For the sphere the coordinate origin is at the sphere center, x is downstream and y and z are the lateral coordinate axes. The polar angle ϕ is zero at the flow stagnation point and 90^o at the $y - z$ plane.

Preliminary results on grid Sphere-1 showed that the lateral force power spectral density (PSD) had no shedding signature as would be expected. It was reasoned that the shedding vortices were diffusing too soon in the wake, and therefore, were not able to exert sufficient fluctuating pressures on the sphere surface. The grid in a cone directly downstream of the sphere body was refined with an average cell size $0.05D$. This grid, Sphere-2, is shown in Figure 1(b). Sphere-1 and Sphere-2 have 1.62×10^6 and 2.79×10^6 cells, respectively.

In this paper we report primarily on grid Sphere-2. Several other grids were developed, including one with 20×10^6 cells for which the super-critical Reynolds numbers was fully-resolved. We have not finished running that grid.

On the sphere surface a no-slip boundary condition is applied to the velocities and the wall-normal pressure gradient is set to zero. A constant velocity boundary condition is applied at the inflow and the cylindrical outer boundary and a continuitive boundary condition is applied at the downstream boundary.

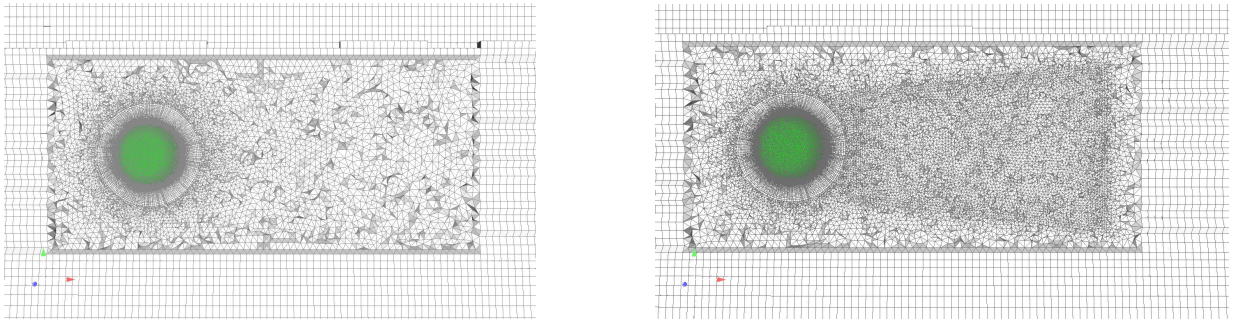

(a) Sphere-1 (b) Sphere-2

Figure 1. Meshes for sphere showing only part of the computational domain.

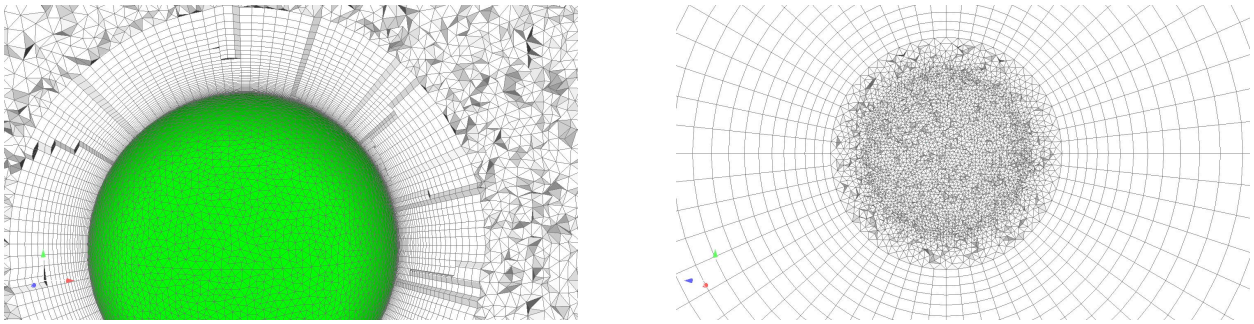

(a) Surface grid and prism layers. (b) Constant-x cut downstream of sphere.

Figure 2. Details of Sphere-2 grid.

We experimented with a number of time step sizes, comparing transverse force PSD. A time step size $0.005D/U$ gave us decent throughput, resolved the shedding peak and maintained a CFL number well less than 1.0. The simulations were run for a minimum of $200D/U$ in order to obtain enough time series data to resolve the low-frequency portion of the power spectral density (PSD).

B. ASDS

The Advanced SEAL Delivery System (ASDS) is a small submersible with a streamlined bow transitioning to a parallel middle body with a rounded rectangular section shape and a fairly streamlined stern. The length, height and width of the body are $L_a = 43.02$, $h = 5.45$ and $w = 4.46$ grid units respectively where a grid unit $\ell_{gu} = 5.08$ cm. The x-axis is in the flow direction with the bow and stern of the model located at $x = 96.95$ and 140.0, respectively. The y-axis has its origin on the ASDS centerplane and is positive to starboard. The z-axis is positive upward with the ASDS mid-plane at $z = 21$. As can be seen in Figure 3(b) the nose geometry is quite a bit more streamlined than a semi-circular geometry shown with the dotted lines. The semi-circle geometry has been shown to generate leading edge separation.[19] The ratio of corner radius to beam $r/w = 0.14$. The transition from the parallel middle body to the stern is accomplished by a continuous curve (as opposed to a sharp change in slope for the Ahmed body) into a 17.6^o slope.

The barehull ASDS volume meshes are structured hexahedral grids with a C-O grid topology as shown in Figure 4(a). All grids maintain a $1.2\Delta^+$ wall-normal spacing at the wall, with $48\Delta^+$ streamwise and $12\Delta^+$ girthwise spacing (based on the approximation that $u_\tau = 0.04U_o$). This resulted in the three grids as listed

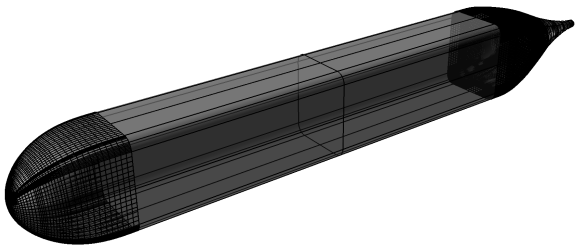

(a) Rendering of ASDS geometry with partial view of surface grid.

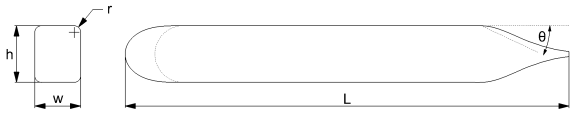

(b) ASDS model geometry. The solid bow line is the actual ASDS bow; dotted line at the bow is a half-circle. The 25^o stern angle for one of the Ahmed bodies is shown. The actual stern angle for ASDS is 17.6^o.

Figure 3. ASDS geometry.

in Table 1. Figure 4(b) shows grid details for Grid-15 in a constant-x cut through the parallel middle body. Figure 4(c) and (d) show details of the grid at the bow and stern, respectively. The figures show that with the C-O topology a high degree of orthogonality is maintained throughout the grid. Grid-16 and Grid-17 have similar topology, but tighter spacings and are not shown.

The time step size for the simulations was $0.01\ell_{gu}/U_o$ so that approximately 4300 time steps were required for the flow to process one body length. This gives a CFL number much smaller than 1.0. The simulations were typically run for at least 10 body lengths to resolve low-frequency shedding. ASDS simulations were run on HPC cluster "Humvee" a Linux Networx Advanced Technology Cluster and NSWCCD's SEATech Center "Nile" a Penguin Computing Cluster. The computational information for the simulations is shown in Table 1. The table shows the number of processors and cluster that each simulation was run on, the CPU time per time step and the number of CPU hours per body length. It can be seen that for each two-fold increase in Reynolds number the grid size increases by factors of 5 and 5.75 between Grid-15 and Grid-16 and Grid-16 and Grid-17, respectively. The CPU times increase by approximately 6 and 18 between the two sets of simulations, respectively. Piomelli and Balaras[20] reason that the grid size for fully-resolved LES should increase by $Re^{1.8}$ which means that for a doubling in Reynolds number the problem size will increase by a factor of 3.5. This is smaller than our grid size increases. They also show that the computational demands should increase by $Re^{2.4}$, which means that for a Reynolds number doubling, a 5.3-fold increase in computing time should be expected. Our increase of 6 and 18 in total CPU time is much larger than this.

Table 1. Grid designations, grid sizes, Reynolds number and computional parameters for ASDS simulations. Re is the Reynolds number based on the free stream velocity and the total length of the ASDS, Nprocs=number of processors, WCS/TS=wall clock seconds per time step, CPUH/L=CPU hours per body length.

Grid	No. of cells	Re	Nprocs	Cluster	WCS/TS	CPUH/L
Grid-15	4×10^6	128×10^3	192	Nile	0.8	190
Grid-16	20×10^6	256×10^3	192	Humvee	5	1150
Grid-17	115×10^6	512×10^3	768	Humvee	23	21100

IV. Results

A. Sphere

In this section we will compare results — drag coefficient, separation point, lift and drag PSDs — to experiments and recent LES literature.[3,4] What is novel about this work is that we were able to run for much longer time series than previous LES efforts which allowed us to observe low-frequency wake rotations.

As discussed in the previous section we experimented with a number of grid densities to obtain the correct shedding behavior. Figure 5 show contours of λ_2 for Sphere-1. Previous LES results[3] showed that

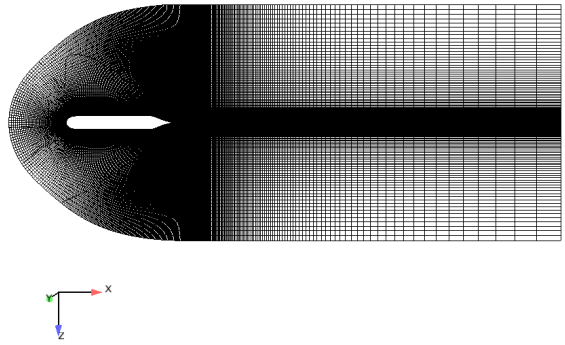

(a) Global view of ASDS Grid-15.

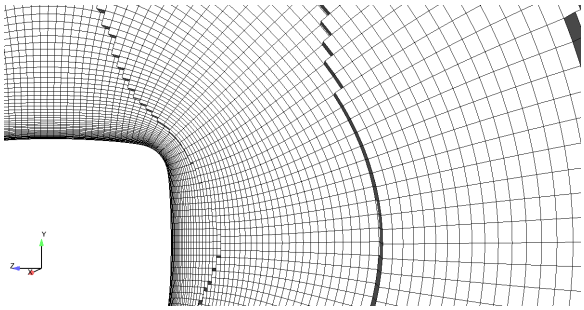

(b) Constant-x cut for ASDS Grid-15

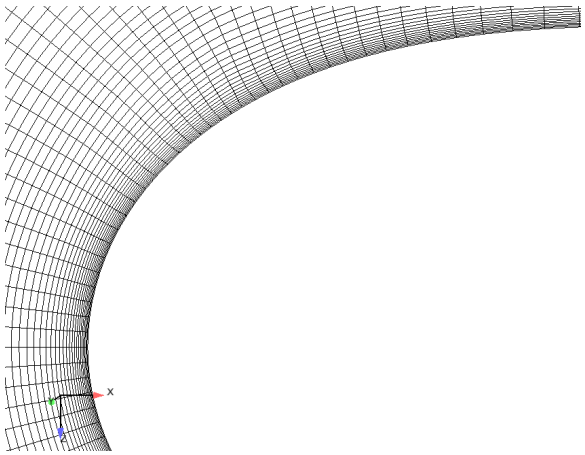

(c) Grid around bow for ASDS Grid-15

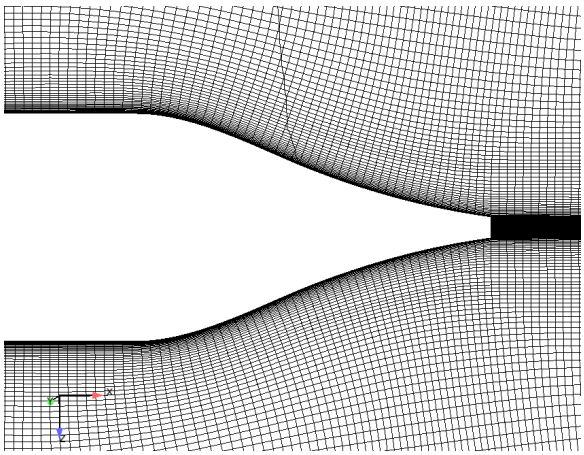

(d) Grid around stern for ASDS Grid-15

Figure 4. ASDS Grid-15.

organized structures may extend $10D$ or more downstream. In the case of Sphere-1, the organized turbulence structures disappear only $1D$ downstream. It was apparent from these iso-surfaces, as well as PSD, that the Sphere-1 grid did not have sufficient grid density in the wake to support the scales of turbulence important to wake dynamics.

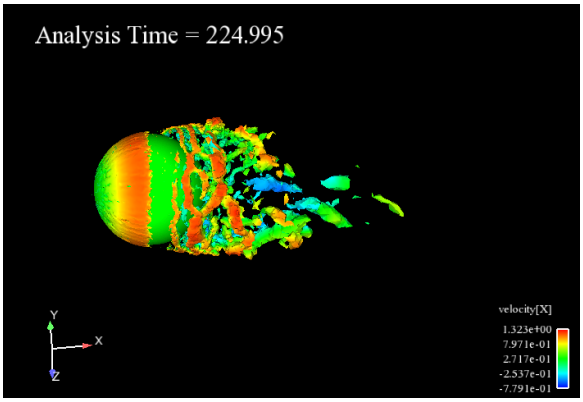

Figure 5. Iso-surfaces of $\lambda_2 = -10$ for sphere-1 for sub-critical case ($Re = 10,000$).

Figure 6(a) is an instantaneous snapshot of axial velocity contours for the sub-critical $Re = 4.2 \times 10^4$ case for Sphere-2. The flow separates around $\phi = 72^o$, earlier than previous results.[3,4,21] The flow on the sphere surface appears to be smooth, and thus can be assumed to be laminar, while the flow in the near-wake is smooth, becoming wavey and then turbulent in the downstream direction. From a qualitative standpoint this is the expected behavior for a sub-critical flow. A large range of turbulence scales has been simulated from δ-scale in the near-wake to D-scale in the far wake. For both sub-critical cases, the separation points appear to be stationary. The pressure contours upstream of the separation point are very stable for $Re = 1 \times 10^4$, whereas for $Re = 4.2 \times 10^4$ the contours have a small amount of movement, indicating that the higher Reynolds number sub-critical case may have instabilities in the "laminar" boundary layers. Note that the wake width is on the order D or greater and that the (blue) region of backwards flow extends relatively far aft of the sphere. The reason for the large wake thickness is that the flow detaches from the sphere as it is increasing in size, and therefore, the shear layer "jets" out at an oblique angle to the free stream flow.

For the sub-critical cases, iso-surfaces of λ_2 show that "ring" vortices with a ring-torus topology are shed from the surface of the sphere. These inner tube-shaped ring vortices can be described by two radii: R, the radius of the center of the tube about the x-axis and r, the radius of the tube. The aspect ratio is defined as R/r. When the ring vortices are first shed they are only quasi-azimuthally symmetric with high aspect ratio. However, r quickly grows as they advect downstream followed by a transformation into hairpin vortices. At about D downstream of the sphere, only very discrete, very large hairpin vortices are visible. The hairpin vortex formation mechanism may be due to those parts of the ring vortices that extend out into the faster moving fluid stretching due to their exposure to the faster moving free stream flows at the edge of the wake. In addition, those portions of the ring vortices that are in the inner wake get pulled backwards into the separation zone directly behind the cylinder. Within the first $2D$ aft of the sphere, a violent merging of hairpin vortices takes place as they get engulfed and/or join with other vortex structures generated in the separation region.

Figure 6(b) shows instantaneous velocity contours for the super-critical case ($Re = 1.1 \times 10^6$). Here, the separation point has moved around to 115^o, consistent with previous results[3,21] that show a 120^o separation point. The wake has narrowed considerably and the recirculation zone in much shorter. The pressure drop upstream of the separation point is much deeper than for the sub-critical cases. Animations show that the low pressure region moves about considerably on order of $d\phi \approx 20^o$, indicating that the flow on the sphere is turbulent. Also, the separation point moves considerably in response to, or perhaps the cause of, the wake trajectory which is constantly changing in a three-dimensional fashion. The shed ring vortices have a much smaller radius r with less azimuthal cohererency than the sub-critical cases. Animations show that the trajectory of the wake changes on the order of $\pm 20^o$ over time periods of the order of approximately $40D/U$ or more. This is consistent with CS who noted that for $Re = 1.1 \times 10^6$ their wake trajectory was at

an oblique angle to the axis of symmetry for their entire $30D/U$ simulation.

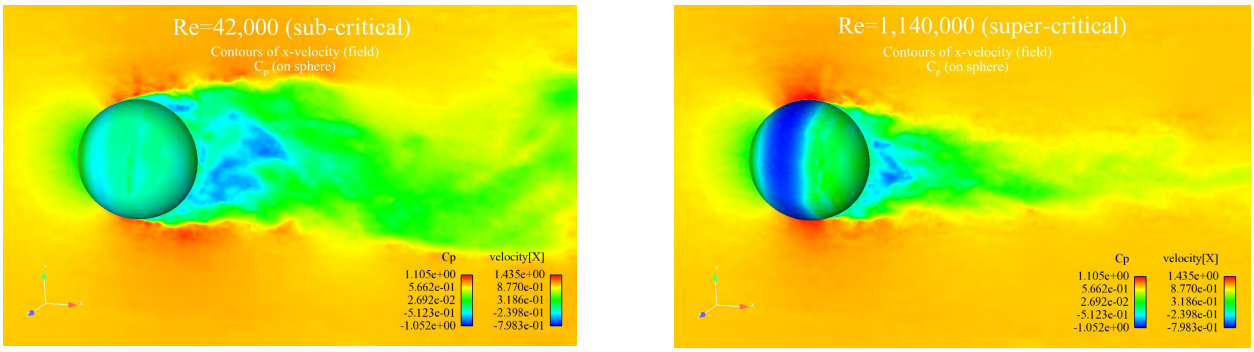

(a) Sub-critical case ($Re = 42,000$) (b) Super-critical case ($Re = 1.1M$).

Figure 6. Instantaneous contours of axial velocity and pressure for sphere.

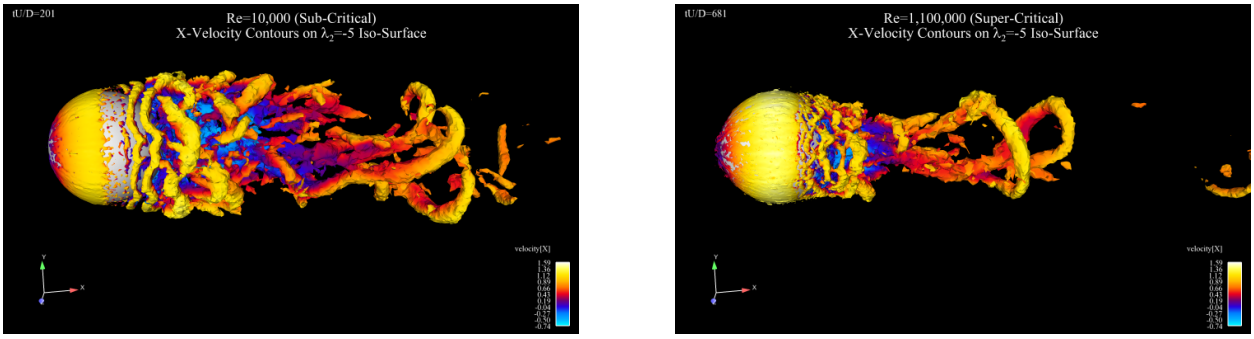

(a) Sub-critical case ($Re = 10,000$) (b) Super-critical case ($Re = 1.1M$).

Figure 7. Instantaneous iso-surfaces of $\lambda_2 = -5$ for sphere.

Time series for total and pressure drag for $Re = 1 \times 10^4$ are shown in Figure 8(a). The viscous drag component is shown in Figure 8(b). It can be seen that the pressure drag comprises most of, and is highly correlated with, the total drag. There appear to be — possibly — four time scales of fluctuations, on the order of $100D/U$ as manifested by the high amplitude drag events at $80D/U$ and $190D/U$, moderate time scales of order $25D/U$ and shorter time scales of length $3 - 5D/U$ and $0.5D/U$. The viscous drag, though much smaller is highly correlated with the total and pressure drag though appears to lag by $2D/U$ the maxima and minima in the total drag. The lag is not surprising as the pressure disturbances in the wake are felt instantaneously on the sphere (since this is an incompressible simulation) while the viscous turbulent structures on the sphere surface itself can only react as fast as the finite viscous time scales, ν/u_τ^2, perhaps through increasing the area of attached flow. This is an area that needs additional research.

The tranvserse force signals, Figure 8(c), dominated by two time scales on the order $25D/U$ and $5D/U$. The side force angle, β defined by,

$$\beta = \tan^{-1}\left(\frac{C_z}{C_y}\right) \tag{1}$$

is shown in Figure 8(d). A negative slope, $d\beta/dt$, denotes a clockwise rotation of the forces as viewed by an observer behind the sphere. For instance, for $110 < tU/D < 140$ the slope is negative and the side forces and, ostensibly, the wake, are spinning slowly clockwise at an average rate of 1 rotation every $60D/U$. There appears to be no predominant rotational direction. The large angle switches between $\beta \pm 180$ are simply due to small changes in β around where the arctan function switches quadrants.

Time series of forces and side force angle for $Re = 1.1 \times 10^6$ are shown in Figure 9. The drag signal is punctuated by high amplitude events that occur on the order of $30 - 50D/U$. The side force angle shows evidence of a clockwise rotation at a rate of 1 rotation per $100D/U$ that, in the mean, persists for $150D/U$ (from $600D/U$ to $760D/U$), punctuated by short-lived changes in direction on the order of $25D/U$.

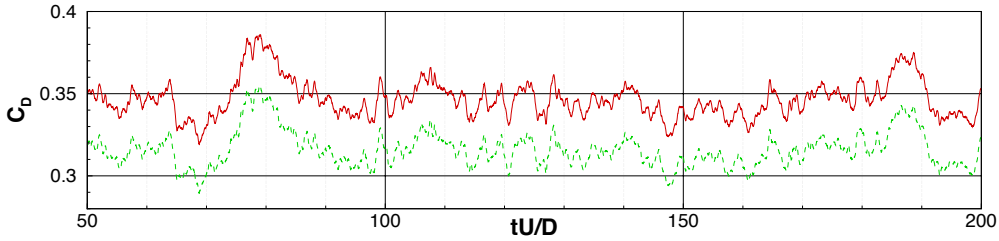

(a) Total (———) and pressure (–) drag.

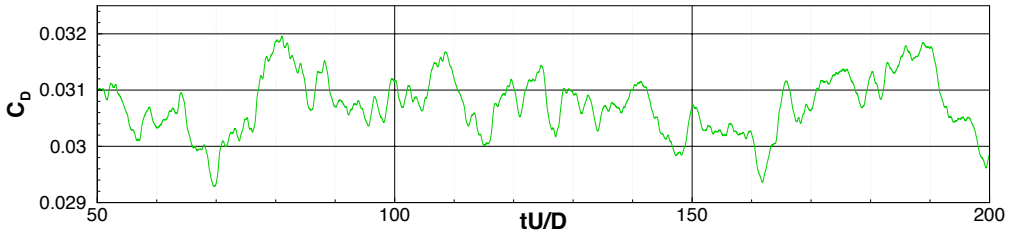

(b) Viscous drag

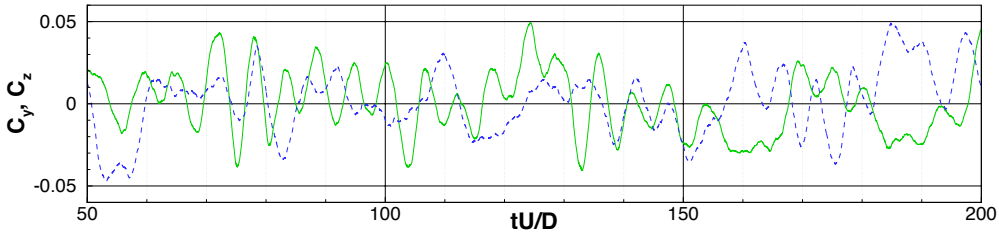

(c) Transverse forces: ——— : C_y; – : C_z.

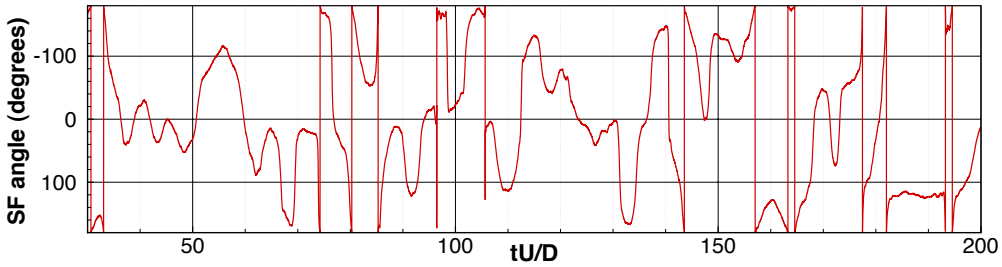

(d) Side force angle.

Figure 8. Force time series for sphere-2 at $Re = 1 \times 10^4$

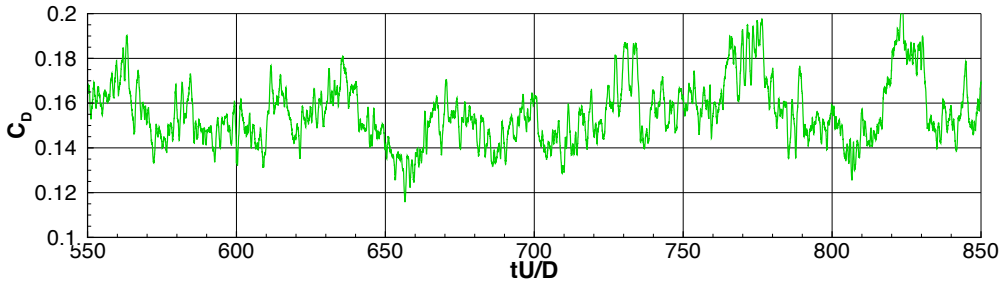

(a) Total drag.

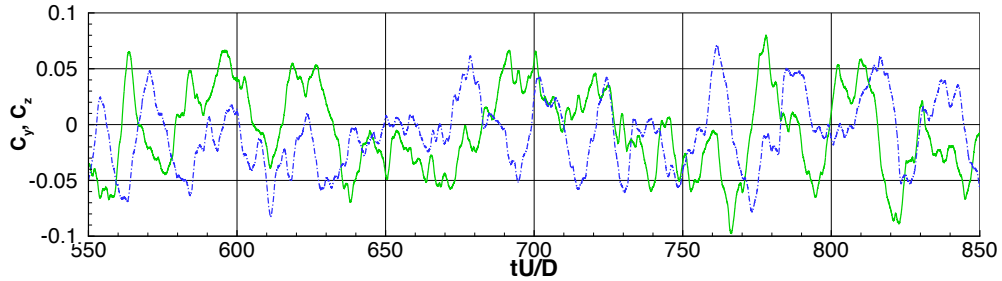

(b) Transverse forces: ——— : C_y; —·— : C_z.

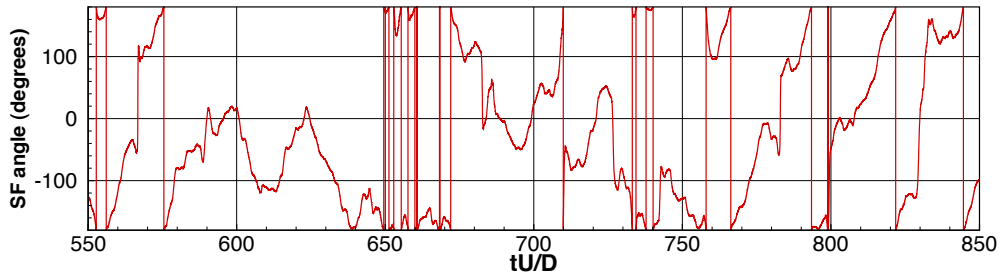

(c) Side force angle.

Figure 9. Force time series for sphere-2 at $Re = 1.1 \times 10^6$

Figure 10, the drag coefficient as a function of Reynolds number, shows that, in general, the present results compare well with experiments and previous LES results. In particular, our results correctly capture the drag crisis at $Re = 3 \times 10^5$ where the drag drops sharply. The sub-critical ($Re = 1 \times 10^4$) drag coefficient $C_D = 0.35$ is low in comparison to experiments[1] ($C_D \approx 0.40$) and CS ($C_D = 0.39$) and Kim[4] ($C_D = 0.43 - 0.44$). As will be discussed later, our lower drag values are due to earlier flow separation.

While we correctly predict the drag crisis, our value of $C_D = 0.15$ at $Re = 4.2 \times 10^5$ is higher than the experimental value of ≈ 0.09. The over-prediction of drag is due to slightly early separation and and will be discussed later. It can be seen that for $Re > 3.7 \times 10^5$ the C_D values predicted by CS with a turbulent boundary layer (TBL) are very close to the experimental values. However, for $Re = 1 \times 10^5$ their results with TBL are low in comparison to experiments due to a flow separation further downstream than experiments. Interestingly, the laminar boundary layer (LBL) results of CS correctly predict the drag crisis but then continue to decrease with Reynolds numbers contrary to experimental results.

While CS introduce a small amount of turbulent viscosity into their calculation at super-critical Reynolds numbers, we allow turbulence to develop naturally. It can be seen in animations and Figure 7 that at the super-critical Reynolds numbers the flow does appear to transition to turbulence on sphere surface, the flow detachment location varies with time and flow in the near-wake shear layers have velocity fluctuations when they detach from the surface.

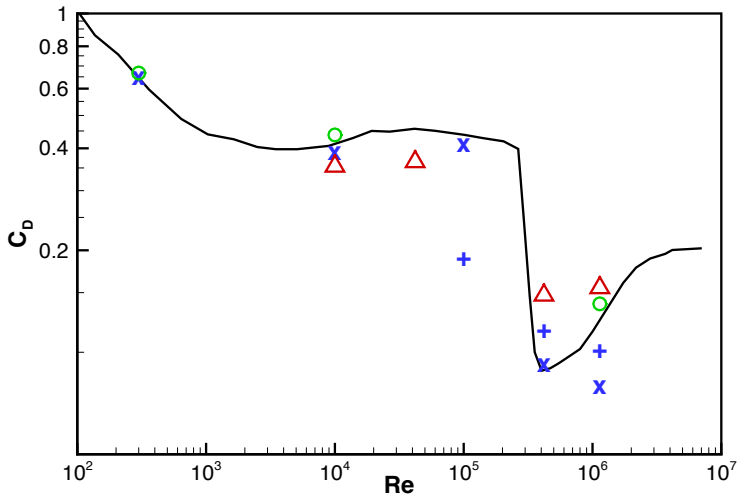

Figure 10. Sphere drag coefficient as function of Reynolds number; △ : present study; ——— : experiment;[1] + : CS[3] turbulent boundary layer; × : CS[3] laminar boundary layer; ○ : Kim.[4]

Table 2 lists the separation points compared with the results of CS and experiments. The separation point is defined as the point on the sphere where the time- and azimuthally averaged shear stress is zero. The separation points for $Re = 1 \times 10^4$ and $Re = 4.2 \times 10^4$ are 74^o and 72^o, respectively which are earlier than experimental[21] values of 83^o and CS[3] and Kim.[4] The reason for this this early separation is under investigation.

The separation points for the super-critical cases, $Re = 4.2 \times 10^5$ and $Re = 1.1 \times 10^6$ are 104^o and 115^o, respectively, jumping sharply from the sub-critical values as the flow on the sphere surface undergoes transition to a more stable turbulent boundary layer. The values are slightly less than the experimental values, which could be due to grid under-resolution. We note that the separation angles obtained by CS for both the sub- and super-critical cases are very close to the experimental values. In their investigation they showed that the separation location is highly dependent upon whether or not, and where (ϕ), the Spalart-Allmaras turbulence model is turned on.

The time and circumferentially-averaged polar pressure distributions are shown in Figure 11 for the sub- and super-critical cases. The C_p values, for both sub-critical Reynolds numbers, Figure 11(a), are slightly above those for CS (At time of writing experimental C_p data of Achenbach[21] was unavailable, but

Table 2. Separation angle ϕ_s (^{o}) on sphere for LES compared with experiment.

Re	LES	Expt[21]	CS[3]	Kim[4]
1×10^4	74.4	82.5	85	86-87
4.2×10^4	71.8			
4.2×10^5	104	114	118	
1.1×10^6	115.2	120	120	98

is very close to the CS curves). Downstream of the flow separation the pressure is constant at the "base" pressure which is a small negative value. The pressure drag is the integration of the pressure dotted with the streamwise vector, which more heavily weights the pressures nearest to $\phi = 0^o$ and 180^o. The $Re = 1 \times 10^4$ base pressures for our results and CS are very close so the discrepancy between our drag results and CS is not due to the pressure distributions. For both super-critical cases, the C_p distributions fall on top of each other, with the exception of a small difference in the base pressure. The minimum pressure is slightly higher than the results of CS which may be due to the difference between our under-resolved LES boundary layer and the Spalart-Allmaras turbulence model used by CS. Also shown is the "ideal" solution for a sphere in an ideal (non-viscous) fluid. For the ideal case the flow remains attached over the entire body and the pressure recovers to $C_p = 1.0$ at $\phi = 180^o$ which leads to zero drag in the so-called "D'Alembert's paradox." It can be seen that the effect of viscosity is to retard the fluid along the body leading to a smaller magnitude minimum pressure, flow separation and base pressure drag.

For the sub-critical cases, we can deduce that since the pressure distributions show close agreement between our results and CS, the reason for our under-prediction of C_D is due to the viscous stresses. For CS and experiments the attached boundary layer hangs on longer by about 10^o, with the attached boundary layer providing the increase in drag. Since viscous drag is the surface drag dotted with the streamwise vector, it has its greatest impact near $\phi = 90^o$, which is the case for sub-critical separation locations.

On the other hand, the early separation for the super-critical cases leads to slightly *higher* drag. Figure 11 shows that the base pressure assumes its value from where the along the sphere the flow separates. Since for attached flows the pressure is increasing on the back of the sphere, early separation means a lower value of base pressure, and therefore, a greater net force on the sphere afterbody, thus increasing the drag.

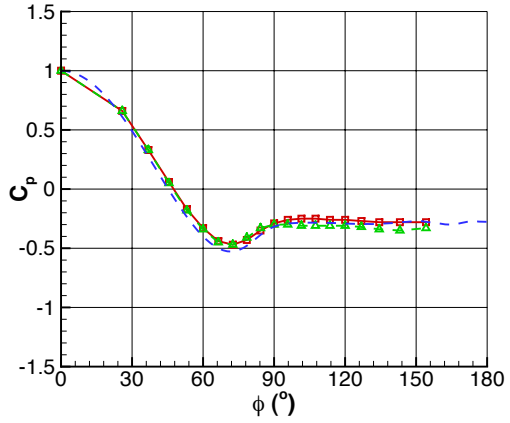

(a) Sub-critical cases; −: CS, $Re = 1 \times 10^4$; □: present results, $Re = 1 \times 10^4$; △: present results, $Re = 4.2 \times 10^4$

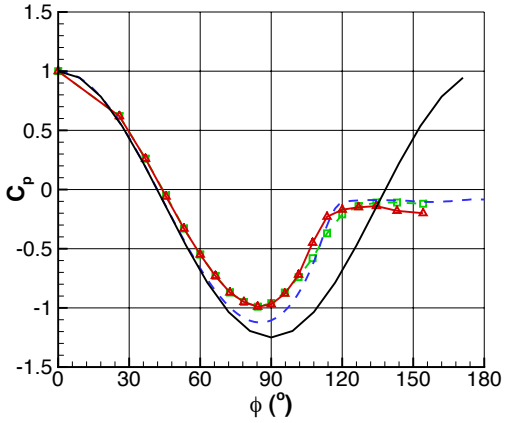

(b) Super-critical case, −: CS, $Re = 4.2 \times 10^5$; □: present results, $Re = 1 \times 10^4$; △: present results, $Re = 1.1 \times 10^6$

Figure 11. Time- and circumferentially-averaged pressure distributions for sphere.

The PSD were computed from a time series of forces that was $400D/U$ long with a time interval $0.01D/U$. The time series was divided into segments of 5000 points each with a 50% overlap, windowed with a Hanning window and then rescaled to maintain the original energy. A fast Fourier transform was then taken and the

amplitude of the complex spectra divided by the frequency resolution gives the PSD. The PSD for each of the time segments were then averaged.

Figure 12(a) shows the drag force PSD for the subcritical cases compared with CS.[3] Our results for the drag forces show a low frequency peak at $St \approx 0.04$, a very small peak at $St = 0.19$ and a very weak, broad band rise at $St \approx 1.5$. The period corresponding to $St \approx 0.04$ is $25D/U$ which shows up fairly clearly in the viscous drag component, Figure 8(b). CS also have a small peak at $St = 0.19$ but have a more prominent peak at $St = 2.05$. CS claim that these two peaks are due to vortex shedding and "Kelvin-Helmholtz instabilities in the detached shear layers," respectively. We suspect that the peak at $St = 2.05$ may be due to the fact that in a "small upstream part of the detached shear layer" CS used an "upwind" discretization. This may have had the effect of reducing random velocity fluctuations while still allowing the generation of coherent ring vortices. Without random fluctuations the vortex ring pinch-off would generate an azimuthally constant axial force on the sphere surface. Figure 7(a) and animations of λ_2 show that in our case the shed ring vortices are azimuthally incoherent. Although they are azimuthally continuous they deviate in the streamwise direction on the order of the streamwise spacing between the rings. This would have the effect of generating an incoherent axial force on the sphere resulting in less energy at the Kelvin-Helmholtz shedding frequency. The experimental data of Achenbach[2] is inconclusive on this subject as their spectral data are only based on hot-wire measurements at a single point 7^o upstream of the detachment point which bears very little relation to the integrated forces over the entire sphere.

Figure 12(b) shows the transverse force (y-component) PSD for the subcritical cases. For $Re = 1 \times 10^4$ there are relatively narrow band peaks at $St = 0.04$ and $St = 0.17$ which compare very well in frequency and power level with CS. For $Re = 4.2 \times 10^4$ there is a smaller peak at about $St = 0.16$. Table 3 shows results for experiments and previous computations.

Table 3. Sub-critical vortex shedding frequencies for sub-critical Reynolds numbers.

Re	Expt[2]	LES	CS[3]	Kim[4]
1×10^4	0.14-0.16	0.17	0.17	0.18
4.2×10^4	0.17-0.18	0.16		

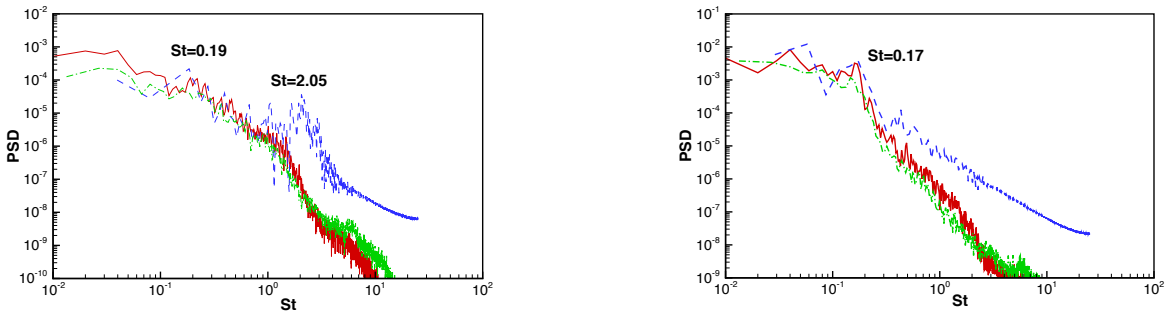

(a) Axial force

(b) Transverse force

Figure 12. Force PSD for sphere at sub-critical Reynolds numbers; ——— : present study ($Re = 1 \times 10^4$); —·— : present study ($Re = 4.2 \times 10^4$); – – – : CS ($Re = 1 \times 10^4$)

Achenbach[2] notes that for $Re > 3.7 \times 10^5$ the shedding signature as measured by a surface mounted hot wire probe upstream of the mean separation point abruptly disappears. In other words, once the flow on the sphere becomes turbulent there are no discernible periodic excitations either from ring vortex or wake shedding. Figure 13 show the drag and tranverse (y-component) force PSD for the super-critical case $Re = 1.1 \times 10^6$. Except for low frequency peaks at $St \approx 0.04$, the PSD falls off monotonically which is consistent with Achenbach.[21] This is in contrast with CS whose data has prominent peaks at $St = 1.3$ and $St = 0.23$ for the drag and transverse forces, respectively. CS provide no explanation for the peaks in drag force spectra. Their peak in the transverse PSD is close to where a vortex shedding peak may be. We note that our super-critical simulations are under-resolved since we used the same grid for both sub- and

super-critical cases. A fully-resolved super-critical simulation is necessary to validate our results. The peak at $St = 0.04$ corresponds to a $25D/U$ period. The transverse force time series show that that high amplitude peaks occur with about this periodicity.

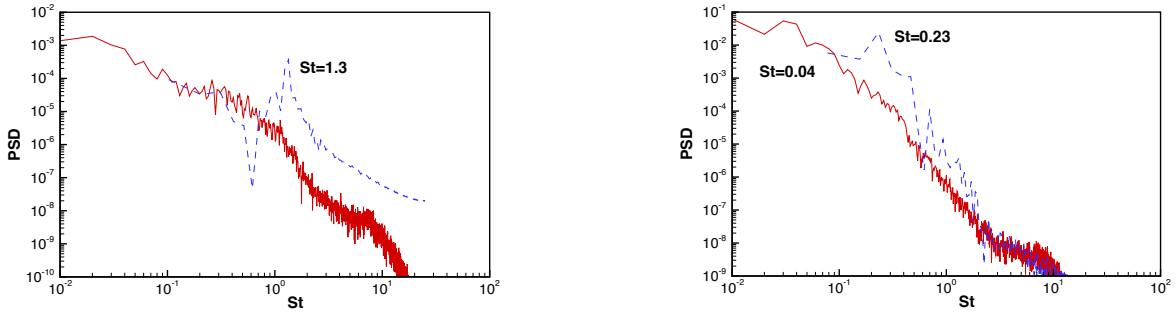

(a) Axial force

(b) Transverse force

Figure 13. Force PSD for sphere at super-critical $Re = 1.1 \times 10^6$; ——— : present study; − − − : CS.

B. ASDS

In this sub-section we will discuss results from fully-resolved LES of barehull ASDS at three Reynolds numbers. Although there is no data to directly compare with we compare to developing boundary layer investigations for flows with bypass transition and leading edge separation. We find that our results are physically reasonable.

Figure 14 shows instantaneous velocities and Figure 15 shows mean velocity contours at the z-symmetry plane for the three Reynolds numbers. The instantaneous velocity contours show that the flow is laminar at the bow, has a section with laminar boundary layer, transitions to a developing turbulent boundary layer, accelerates around a stern knuckle and then separates in the stern. In these simulations the inflow velocity fields have a zero turbulence level so the laminar-turbulent transition is set up naturally by the slightly adverse pressure gradient aft of the bow (the minimum $C_p \approx -0.5$) and the laminar velocity profiles there. The details of the actual transition cannot be resolved. Nonetheless, as we show later, the boundary layer parameters as scaled by Re_x are consistent with flows that undergo leading edge separation and bypass transition.[19] The physical location of the transition appears further upstream with increase in Reynolds number, which is reasonable since the location of the transition point is dependent upon the viscous length scales, $\Delta^+ = \nu/u_\tau$, which decrease with Reynolds number. As expected, the boundary layer thickness and the size of the turbulence fluctuations along the hull decrease in size with Reynolds number.

Figure 15(a) shows that for the lowest Reynolds number case separation occurs directly aft of the stern knuckle and the separation region completely engulfs the stern. Figure 14(a) shows that the size of the spanwise vortices is on the order of one-half the height. The mean velocities Figure 15(a) are not symmetric about the y-symmetry plane probably because we did not average over sufficient samples.

The mean velocities, Figure 15, show that with increasing Reynolds number the location of separation moves aft and the size of the recirculation zone shrinks. In fact, for the highest Reynolds case, the flow may actually reattach. The fluctuating velocity contours show that the eddies in the separated flow region decrease size with Reynolds number. Animations show that the turbulence structures in the separated flow region exhibit a complex structure with small azimuthal-oriented vortices in the outer shear layers and longitudinal structures dominating the separated flow region.

Figure 16 shows a constant-x cut along the parallel middle body for the three Reynolds numbers. It shows that the boundary layer is thickest towards the center of the flat sections, but decreases rapidly toward the rounded corners. As Reynolds number increases this effect is more muted as the boundary layer thickness increases at the corners while it decreases in the flat sections. Krajnovic et al.[12] in their LES of a very blunt-nosed, simplified bus geometry show that streamwise vortices occur on the corners. However, these may have been set up by flow separations at the front of the bus. We have no explanation for the accelerated flows at the corners except to note that the corners act like extremely large bumps that protrude out into the free stream flow.

(a) $Re = 128 \times 10^3$

(b) $Re = 256 \times 10^3$.

(c) $Re = 512 \times 10^3$.

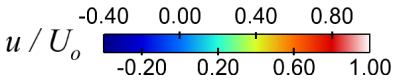

Figure 14. Contours of instantaneous axial velocity (u/U_o) for ASDS at three Reynolds numbers. Slices taken at z-centerplane.

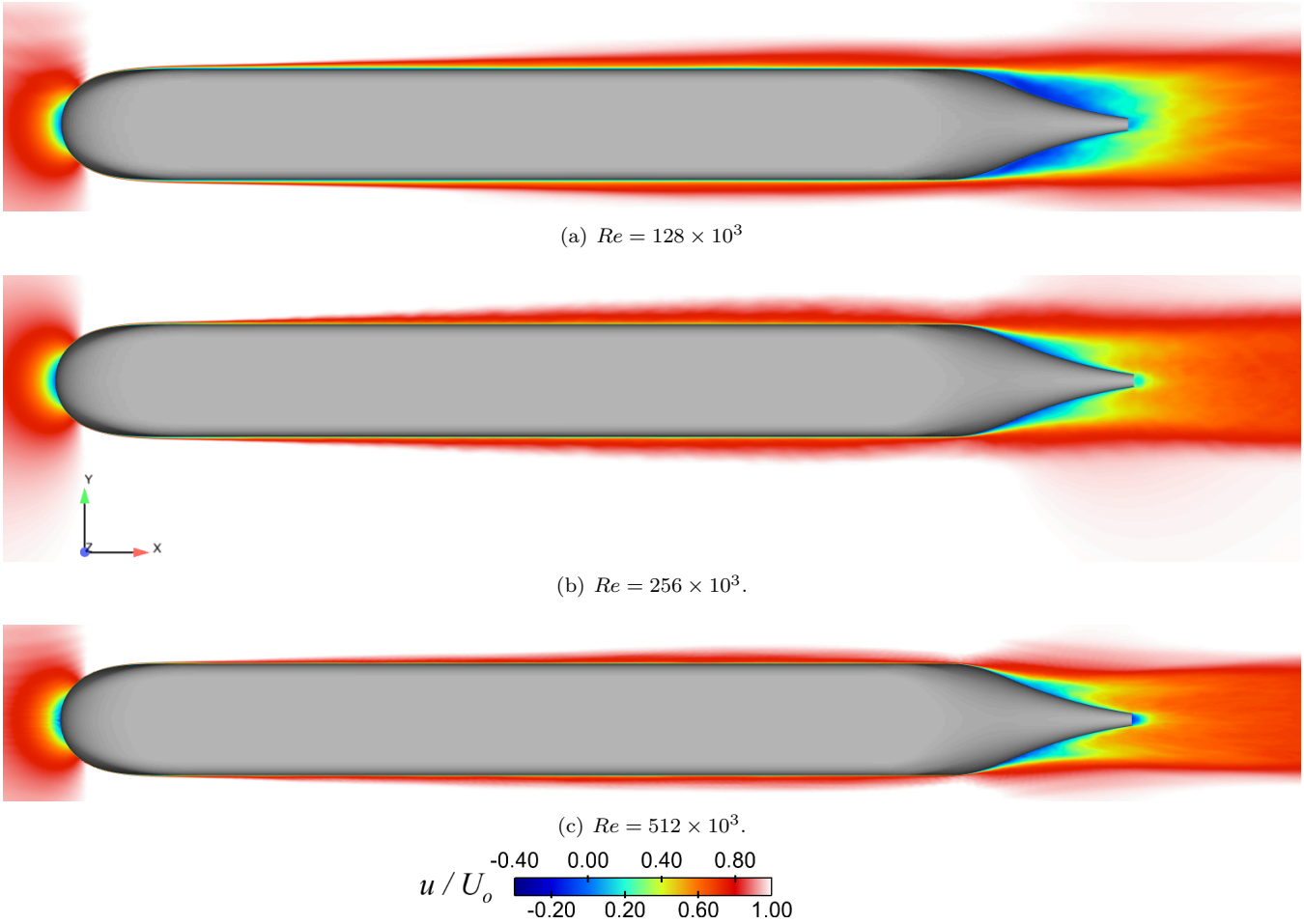

(a) $Re = 128 \times 10^3$

(b) $Re = 256 \times 10^3$.

(c) $Re = 512 \times 10^3$.

Figure 15. Contours of mean velocity (U/U_o) for ASDS at three Reynolds numbers. Slices taken at z-centerplane.

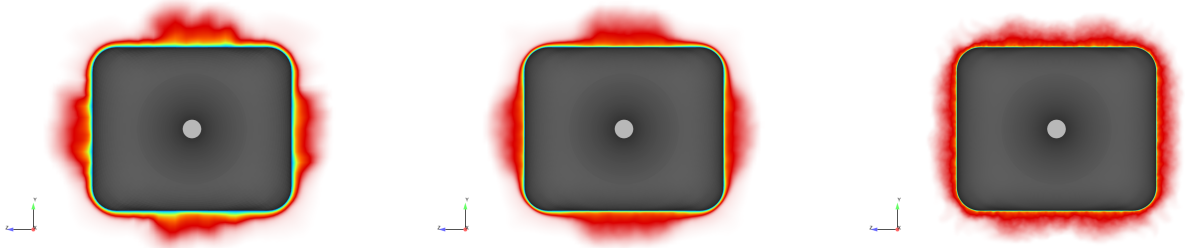

(a) $Re = 128 \times 10^3$

(b) $Re = 512 \times 10^3$.

(c) $Re = 512 \times 10^3$.

Figure 16. Mean streamwise velocity contours at $x = 125$ ($\xi/L_a = 0.65$) for ASDS at three Reynolds numbers.

The velocity profiles for $Re = 256 \times 10^3$ at the z-centerplane are shown in Figure 17 at four x-locations on the parallel middle body, $\xi/L_a = 0.186$, $\xi/L_a = 0.303$, $\xi/L_a = 0.419$ and $\xi/L_a = 0.651$, where $\xi/L_a = 0$ is the bow and $\xi/L_a = 1$ is the stern. Figure 17(a) shows the outer-scaled profiles of U/U_{max} versus y/δ where U and U_{max} are the mean and maximum mean streamwise velocities and δ is the boundary layer thickness i.e., where $U = 0.99U_{max}$. Near the bow the profile is closer to a parabolic profile as would expected for a flow that has just transitioned from a laminar flow; the profiles further downstream become increasing full as higher momentum outer flow is advected toward the wall by turbulent diffusion. Figure 17(a) shows the inner-scaled profiles as compared with the law of the wall, where for $y^+ < 11$,

$$u^+ = y^+ \tag{2}$$

and for $y^+ > 11$,

$$u^+ = \frac{1}{\kappa}\log(y^+) + B \tag{3}$$

$\kappa = 0.41$ and $B = 5.2$. The inner-scaled profiles show that the velocity profiles approach a logarithmic profile with distance from the bow. It has been claimed by Yang et al.[19] that it can take up to 70 boundary layer thicknesses or 7 leading edge separated flow bubble lengths to re-establish the logarithmic behavior downstream of a separation. For $Re = 256 \times 10^3$ the location $\xi/L_a = 0.65$ is only about 20δ downstream from the bow.

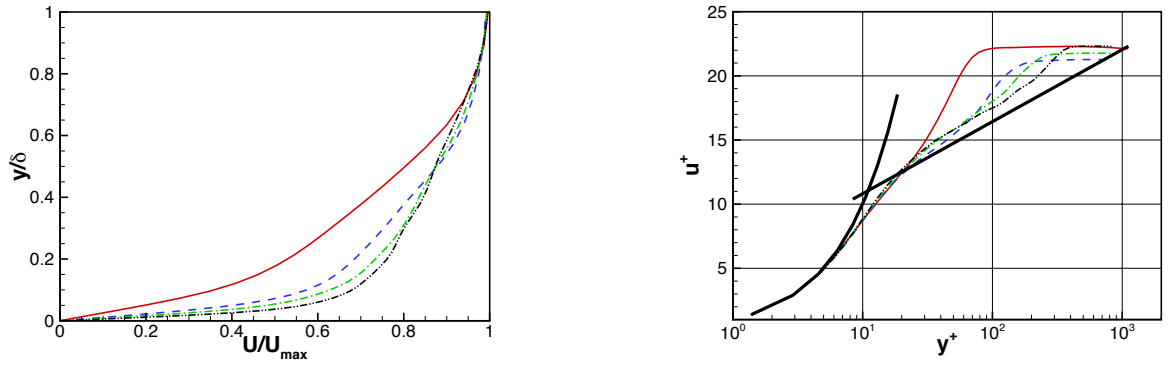

(a) Outer-scaled velocity profiles.

(b) Inner-scaled velocity profiles.

Figure 17. Mean velocity profiles at centerplane for ASDS at $Re = 256 \times 10^3$**:** ——— **:** $\xi/L_a = 0.19$**;** — — — **:** $\xi/L_a = 0.303$**;** —·— **:** $\xi/L_a = 0.419$**;** —··— **:** $\xi/L_a = 0.652$

Table 4 lists some of the boundary layer parameters at three stations along the hull. As there are no natural geometric length scales for a developing boundary layer flow we use $\log(Re_x)$ as the streamwise length scale which commonly appears in the literature[19,22] for spatially developing boundary layer flows. Here, Re_x is based on the distance from the bow and free stream velocity. The shape factor, H, is the ratio of the displacement and momentum thicknesses which has a value of 3.2 for a laminar (Blasius) flat plate boundary layer flow and 1.6 for a "Klebanoff" fully-developed turbulent flat plate boundary layer flow.[23] Yang[19] shows that for a flow with leading edge separation, H undergoes a sharp decrease at $\log(Re_x) = 4.8 - 5.0$ down to an equilibrium value $H \approx 1.5$. Yang also shows that for a flat plate with bypass transition triggered by free stream turbulence H more slowly approaches the turbulent boundary values. Our results show a sharp drop from the laminar value greater than 3 to a value very close to that for bypass transition on a flat plate.[19] Figure 18(b) shows the variation in $\log(C_f)$ with $\log(Re_x)$. Yang[19] shows that downstream of a leading edge flow separation or for bypass transition on a flat plate the $\log(C_f)$ approaches a value of about -2.3 at $\log(Re_x) = 5.1$. Keating et al.[24] report a value $\log C_f = -2.3$ for zero pressure gradient boundary layer at $Re_{\delta^*} = 1000$. Our results, at $Re_{\delta^*} = 1000$ are very close to the same level.

Figure 19 shows fluctuating streamwise velocity contours for $Re = 256 \times 10^3$ at three constant-y layers. Figure 19(a) shows velocity contours in the viscous shear layer, $y^+ \approx 5$. Vertical lines separated by $\Delta x = 5$ representing approximately $1400\Delta^+$ are shown for scale. The horizontal lines represent the outline of the hull, which is about $1600\Delta^+$. As expected that streamwise velocity profiles are long, streaky structures where positive and negative regions alternate in the spanwise direction. The streamwise length scales are on

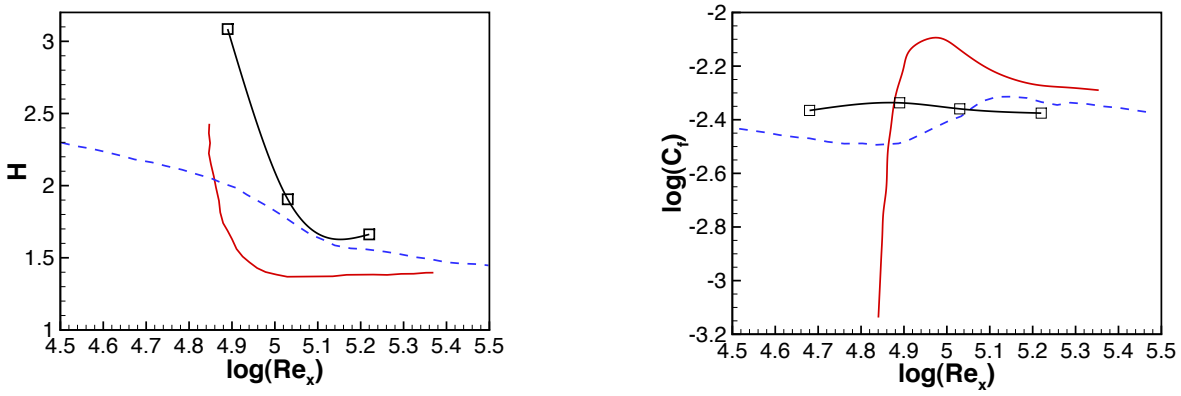

(a) Shape factor.

(b) Friction coefficient.

Figure 18. Mean boundary layer parameters for $Re = 256 \times 10^3$ compared with Yang:[19] □ : present data, ——— : Yang[19]semi-circular leading edge, – – : Yang[19] flat plate.

Table 4. Boundary layer characteristics for attached flow at selected locations along top of ASDS at $Re = 256,000$.

x	ξ/L_a	$\log(Re_x)$	Re_{δ^*}	Re_θ	H	u_τ/U_o	$\log(C_f)$
110	0.303	4.890	422	137	3.09	4.798×10^{-2}	-2.34
115	0.419	5.031	668	350	1.91	4.675×10^{-2}	-2.36
125	0.652	5.222	952	573	1.66	4.590×10^{-2}	-2.38

the order of $500 - 2000\Delta^+$ while the distance between regions of like sign are on the order of $100\Delta^+$. These length scales are similar to what has often been reported in the literature (cf. Robinson[25]). Note that there are virtually no velocity fluctuations at the spanwise extents of the hull.

Figure 19(b) shows the velocity contours in the buffer layer, at $y^+ \approx 24$. In contrast to the contours in the viscous shear layer the contour shapes are slightly wider in the spanwise direction and shorter in the streamwise direction.

Finally, Figure 19(c) shows the velocity contours in the logarithmic layer, at $y^+ \approx 100$. Here the structures are yet fatter in the spanwise direction and shorter in the streamwise direction.

A constant streamwise cut at $x = 110$, Figure 20(a), shows fluctuating streamwise velocity contours and transverse plane velocity vectors. The vertical lines are spaced $\Delta\zeta = 0.5$ apart which represents about $135\Delta^+$. The spanwise spacing between regions of negative velocity fluctuations is about $120 - 150\Delta^+$ and the vertical extent of the turbulence fluctuations at the centerline (demarcated CL) is about $150 - 200\Delta^+$. It has been discussed in the literature[25] that high speed streaks near the wall are the result of "sweeps" which are caused by quasi-streamwise vortices advecting faster moving fluid from the outer boundary layer into the near-wall region. In Figure 20(a) we see several examples of this: a large clockwise vortex centered at $\zeta = -0.8$ sweeping a large region of faster moving fluid onto the wall (centered at $\zeta = -1.2$). On the centerline we see an "ejection" of slow moving fluid being ejected from the wall. Away from the centerline there is a sharp dropoff in turbulence activity.

Figure 20(b) is a transverse cut at $\zeta = -1.0$ where it cuts through the right side of the streamwise vortex discussed in the last paragraph. The vertical lines are separated by $\Delta x = 1.0$ which represents $270\Delta^+$. Contours of spanwise (z) fluctuating velocity are shown, where the positive (red) regions are coming out of the page. In this view is can be seen that the boundary layer is populated by alternating regions of high and low speed spanwise velocity which are manifestations of quasi-streamwise vortices. Also shown are vectors of fluctuating streamwise and vertical velocity components. In the literature the quasi-streamwise vortices have often been shown to slope upwards at about a 23^o angle[20] ending in a "head" which is a spanwise vortex.[25] Our data shows that there may be a weak spanwise vortex at the right of the figure. However, at

least in this limited sample set, the spanwise vortex heads are not a dominant turbulent flow feature. What is apparent from the vector fields is the highly erratic nature of wall shear stress. Recall that shear stress is proportional to the wall normal gradient of the total velocity. Thus, in regions where the vectors are zero, the mean stress is being felt, and regions with positive velocity the turbulence is generating more than the mean stress and where there is negative velocity, less than the mean stress. It is apparent from the figure that in most cases the shear stress in the flow direction is due to sweeps which bring faster moving fluid close to wall increasing the wall normal velocity gradient and drag. This is consistent with the findings of Moin et al.[26]

One of the objectives of this work was to determine whether the near-wall boundary layer turbulence structures from the upstream attached flow regions have a significant influence on the separated flow region. We have not had time to pursue a rigorous study of this subject. However, from perusing animations of velocity contours for the three Reynolds number cases it is evident that the larger turbulence structures, when advecting over the stern knuckle have the effect of pushing the separation inception point downstream, reducing the size of the separated flow region. These types of interactions would not occur if a detached eddy simulations (DES) or wall model approach were used in the upstream attached flow region. These methods model the turbulence structures and while the mean flow dynamics in the attached flow region are correct, turbulent eddies in the separated flow region are only generated if there is an unstable shear layer, e.g., at a sharp surface discontinuity.

Wall modeling and DES approaches are necessary for simulating Reynolds numbers for most engineering applications. In the future we will use our ASDS database for validating such methods.

V. CONCLUSIONS

OUR interest lies in being able to predict the correct separated flow behavior for stern geometries which have weakly separated flows. The applications of these techniques may be in prediction of drag, propeller inflow for hydro-acoustics and structural vibrations. It is hypothesized that much of the energy in the separated flows is advected from the upstream near-wall turbulence structures. Therefore, resolution of the upstream flow is important for making high-fidelity engineering predictions in the stern.

In this exploratory study we performed LES of a sphere at sub- and super-critical Reynolds numbers and found that we obtain physically reasonable results. We show that without external forcing or ad hoc turbulence switching the flow on the sphere maintains the correct Reynolds number dependent laminar or turbulent behavior. At sub-critical Reynolds numbers the flow on the sphere remains laminar, only becoming turbulent in the wake. For super-critical Reynolds numbers the flow on the sphere transitions to turbulence which enables the flow to remain attached longer, thus correctly predicting the drag crisis. We take advantage of long run times to show that the wake rotates very slowly at rates approaching $100D/U$ for one rotation.

We perform fully-resolved LES of flow over a bare hull submersible, the ASDS. For length-based Reynolds numbers from 128×10^3 to 512×10^3 we run with grids from 4 million to 115 million cells. We compare data to developing boundary layer literature and find that it compares quite well. We take an in-depth study of the instantaneous near-wall boundary layer turbulence structures and find that they agree in length scales and kinematics to previous studies of near-wall boundary layer and channel flow turbulence. Due to time constraints we were not able to fully characterize the stern separated flows

VI. ACKNOWLEDGEMENT

WE would like to thank our Office of Naval Research sponsors Drs. Ron Joslin and David Hess for providing funding through the Multi-body dynamics program. The computations were made possible through a Grand Challenge Grant (C3U) of high performance computing time at the Army Research Laboratory, Aberdeen, MD on the Humvee Linux Networx Cluster. We also used the NSWCCD SeaTech Center Penguin cluster, Nile. We would like to thank the support staff at ARL and the NSWCCD SEATech Center. We are appreciative of Professor Georges Constantinescu for sharing data on sphere simulations and to Marvin Sanchez de Losada (NSWCCD Code 5100) for providing the drawings of ASDS.

References

[1]Schlichting, H., *Boundary-Layer Theory*, Physics and Astronomy Online Library, Springer-Verlag, Berlin, 8th ed., 2000.

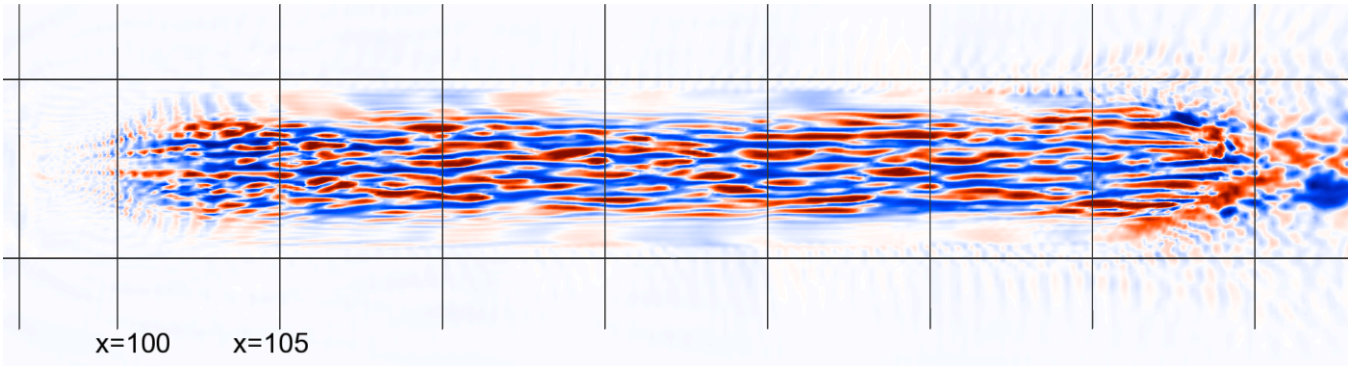

(a) Viscous shear layer ($y^+ \approx 5$).

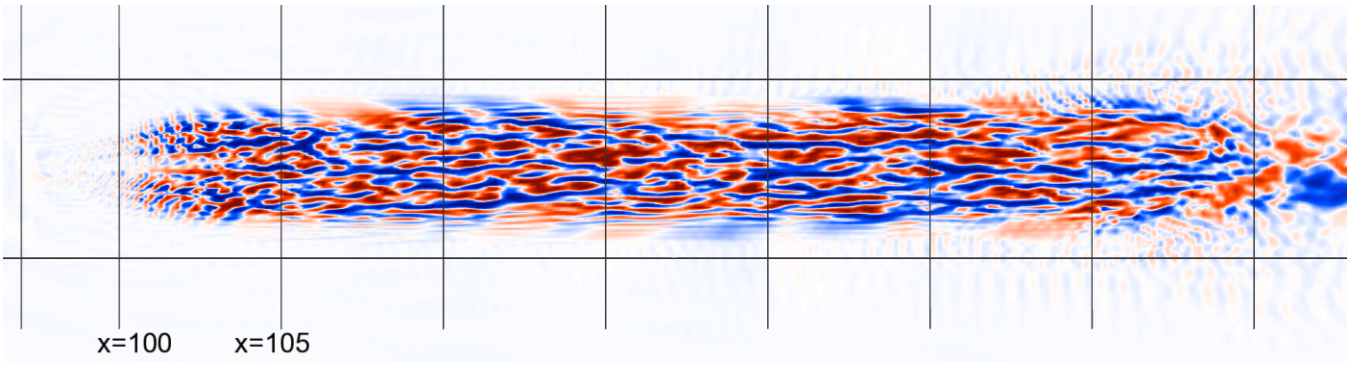

(b) Buffer layer ($y^+ \approx 24$).

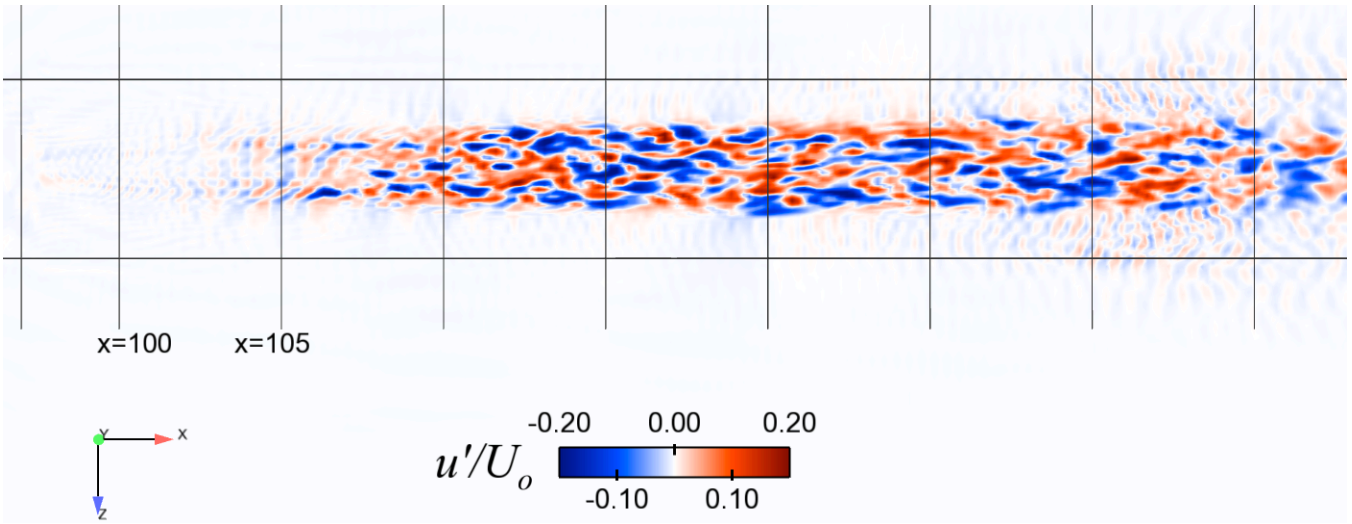

(c) Log layer ($y^+ \approx 100$).

Figure 19. Fluctuating streamwise velocity contours in planes of constant-y for ASDS at $Re = 256 \times 10^3$. The horizontal lines demarcate the bottom and top of the model or about $1500\delta_\nu$. The vertical lines are spaced $1300\delta_\nu$; the model extends from $x = 97$ to $x = 140$; the stern taper starts at $x \approx 135$.

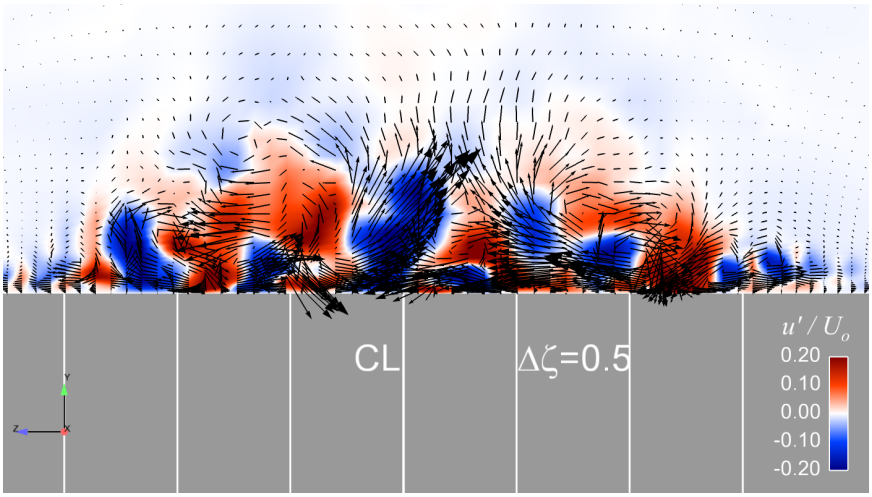

(a) Fluctuating streamwise velocity contours and vectors at $x = 110$ $\xi/L_a = 0.30$. Vertical reference lines are $\Delta\zeta = 0.5$ or $\approx 135\Delta^+$.

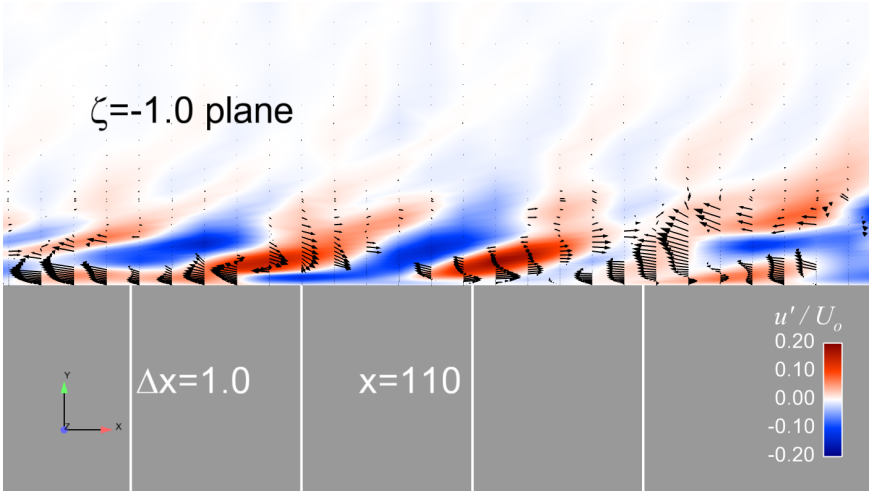

(b) Fluctuating spanwise velocity contours and vectors at $\zeta = 1$. Vertical reference lines are $\Delta x = 1.0$ or $\approx 270\Delta^+$.

Figure 20. Fluctuating velocity contours for ASDS at $Re = 256 \times 10^3$ showing typical turbulence structures.

[2]Achenbach, E., "Vortex shedding from spheres," *Journal of Fluid Mechanics*, Vol. 62, 1974, pp. 209–221.

[3]Constantinescu, G. S. and Squires, K. D., "Numerical investigations of flow over a sphere in the subcritical and supercritical regimes," *Physics of Fluids*, Vol. 16, No. 5, 2004, pp. 1449–1466.

[4]Kim, S.-E., "Large Eddy Simulation Using Unstructured Meshes and Dynamic Subgrid-Scale Turbulence Models," *34th AIAA Fluid Dynamics Conference and Exhibit*, Portland, OR, 2004, p. 17.

[5]Chang, P., Wang, M., and Gershfeld, J., "Prediction of vortex shedding from a high Reynolds number airfoil using LES with and without wall model," *2006 ASME Fluids Eng'g Division Summer Meeting*, Miami, FL, 2006.

[6]Ahmed, S., Ramm, G., and Faltin, G., "Some salient features of the time averaged ground vehicle wake," *SAE*, , No. 840300, 1984.

[7]Minguez, M., Pasquetti, R., and Serre, E., "Spectral Vanishing Viscosity Stabilized LES of the Ahmed Body Turbulent Wake," *Communications in Computational Physics*, Vol. 5, No. 2-4, 2009, pp. 635–648.

[8]Hinterberger, C., M., G.-V., and Rodi, W., "Large eddy simulation of flow around the Ahmed body," *The Aerodynamics of Heavy Vehicles: Trucks, Buses and Trains*, edited by R. McCallen, F. Browand, and J. Ross, Vol. 19 of *Lecture Notes in Applied and Computational Mechanics*, Springer, Berlin, 2004.

[9]Howard, R. and Pourquie, M., "Large Eddy Simulation of an Ahmed reference model," *Journal of Turbulence*, Vol. 3, No. 012, 2002, pp. 18.

[10]Krajnovic, S. and Davidson, L., "Large-eddy simulation of the flow around a simplified car model," 2004.

[11]Verzicco, R., Fatica, M., Iaccarino, G., and Moin, P., "Large Eddy Simulation of a Road Vehicle with Drag Reduction Devices," *AIAA Journal*, Vol. 40, No. 12, 2002, pp. 2447–2455.

[12]Krajnovic, S. and Davidson, L., "Numerical study of the flow around a bus-shaped body," *Transactions of the ASME*, Vol. 125, 2003, pp. 10.

[13]Alin, N., Chapuis, M., Fureby, C., Liefvendahl, M., Svennberg, U., and Troeng, C., "A numerical study of submarine propeller-hull interactions," *28th Symposium on Naval Hydrodynamics*, ONR, Pasadena, CA, 2010, p. 17.

[14]Germano, M., Piomelli, U., Moin, P., and Cabot, W. H., "A dynamic subgrid-scale eddy viscosity model," *Physics of Fluids A - Fluid Dynamics*, Vol. 3, No. 7, 1991, pp. 1760–1765.

[15]Lilly, D., "A proposed modification of the Germano subgrid-scale closure model," *Physics of Fluids A*, Vol. 4, No. 3, 1992, pp. 633–635.

[16]Mahesh, K., Constantinescu, G. S., and Moin, P., "A numerical method for large-eddy simulation in complex geometries," *Journal of Computational Physics*, Vol. 197, 2004, pp. 215–240.

[17]Henson, V. E. and Yang, U. M., "BoomerAMG: a Parallel Algebraic Multigrid Solver and Preconditioner," *Applied Numerical Mathematics*, Vol. 41, 2002.

[18]Chang, P. A., Ebert, M. P., Mahesh, K., and Shipman, J., "Prediction of high amplitude forces during propeller crashback," *DOD High Performance Computing Modernization Program 2008 Users Group Conference*, Seattle, WA, 2008, p. 11.

[19]Yang, Z. and Voke, P. R., "Large-eddy simulation of boundary-layer separation and transition at a change of surface curvature," *Journal of Fluid Mechanics*, Vol. 439, 2001, pp. 305–333.

[20]Piomelli, U. and Balaras, E., "Wall-Layer Models for Large-Eddy Simulations," *Annual Review of Fluid Mechanics*, Vol. 34, 2002, pp. 349–374.

[21]Achenbach, E., "Experiments on the flow past spheres at very high Reynolds numbers," *Journal of Fluid Mechanics*, Vol. 54, 1972, pp. 565–575.

[22]Voke, P. R. and Yang, Z., "Numerical study of bypass transition," *Physics of Fluids*, Vol. 7, No. 9, 1995, pp. 2256–2264.

[23]Pope, S. B., *Turbulent Flows*, Cambridge, England, 2000.

[24]Keating, A., De Prisco, G., and Piomelli, U., "Interface conditions for hybrid RANS/LES calculations," *International Journal of Heat and Fluid Flow*, Vol. 27, 2006, pp. 777–788.

[25]Robinson, S. K., "Coherent motions in the turbulent boundary layer," *Annual Review of Fluid Mechanics*, Vol. 23, 1991, pp. 601–639.

[26]Moin, P., Kim, J., and Choi, H., "On the active control of wall-bounded turbulent flows," *AIAA 2nd Shear Flow Conference*, AIAA, Tempe, AZ, 1989, pp. 89–0960–1.